Paper has been presented at the

Twenty–Second Symposium on
Quantitative Nondestructive Evaluation
held July 30–August 4, 1995
in Seattle, Washington, USA

and has been published in

Review of Progress in
QUANTITATIVE
NONDESTRUCTIVE
EVALUATION
Edited by Donald O. Thompson
and Dale E. Chimenti
Vol. 15B, pp. 1839–1846, 1996
Plenum Press, New York, USA.

# ULTRASONIC AND ELECTROMAGNETIC WAVE PROPAGATION AND INVERSE SCATTERING APPLIED TO CONCRETE

R. Marklein, K. J. Langenberg, R. Bärmann, M. Brandfaß
Department of Electrical Engineering
University of Kassel
D-34109 Kassel, Germany

## INTRODUCTION

Nondestructive testing in civil engineering (NDT-CE) comprises the application of ultrasonic and electromagnetic wave propagation and inverse scattering. The aims of our current research are threefold:

1. Numerical modeling of ultrasonic wave propagation and scattering in concrete with the EFIT code (EFIT: Elastodynamic Finite Integration Technique) to get a better understanding of the ultrasonic wave phenomena in concrete,
2. application of the elastodynamic vector imaging scheme EL-FT-SAFT to modeled data (EL-FT-SAFT: Elastodynamic Fourier Transform Synthetic Aperture Focusing Technique) to detect delaminations in a metal duct or for thickness determination,
3. application of the electromagnetic vector imaging algorithm HD-POFFIS to measurements in order to locate a metal duct in reinforced concrete (HD-POFFIS: Hertzian Dipole Physical Optics Far-Field Inverse Scattering).

## ULTRASONIC WAVES APPLIED TO CONCRETE

Ultrasonic waves in concrete are governed by Cauchy's equation of motion and the equation of deformation rate [1, 2]. These equations are given in integral form for a finite volume $V$ with the surface $S$ by

$$\iiint_V \frac{\partial}{\partial t}\underline{\mathbf{j}}(\underline{\mathbf{R}},t)\,\mathrm{d}V = \oiint_S \underline{\mathbf{n}}\cdot\underline{\underline{\mathbf{T}}}(\underline{\mathbf{R}},t)\,\mathrm{d}S + \iiint_V \underline{\mathbf{f}}(\underline{\mathbf{R}},t)\,\mathrm{d}V\,, \tag{1}$$

$$\iiint_V \frac{\partial}{\partial t}\underline{\underline{\mathbf{S}}}(\underline{\mathbf{R}},t)\,\mathrm{d}V = \oiint_S \mathrm{sym}\,\{\underline{\mathbf{n}}\,\underline{\mathbf{v}}(\underline{\mathbf{R}},t)\}\,\mathrm{d}S + \iiint_V \underline{\underline{\mathbf{h}}}(\underline{\mathbf{R}},t)\,\mathrm{d}V\,; \tag{2}$$

$\underline{\mathbf{j}}$ is the linear momentum density vector, $\underline{\underline{\mathbf{T}}}$ is the stress second rank tensor, $\underline{\underline{\mathbf{S}}}$ is the strain second rank tensor, $\underline{\mathbf{v}}$ is the particle velocity vector, $\underline{\mathbf{f}}$ is the source of force density, $\underline{\underline{\mathbf{h}}}$ is the source of deformation rate second rank tensor, $\underline{\mathbf{n}}$ is the outward normal unit vector of $S$ and $\mathrm{sym}\,\{\underline{\mathbf{n}}\,\underline{\mathbf{v}}\}$ denotes the symmetric part of the dyad $\underline{\mathbf{n}}\,\underline{\mathbf{v}}$.

We assume concrete as a non-dissipative isotropic inhomogeneous material. According to this the material properties are given by the following constitutive equations

$$\underline{\mathbf{j}}(\underline{\mathbf{R}},t) = \varrho_0(\underline{\mathbf{R}})\underline{\mathbf{v}}(\underline{\mathbf{R}},t)\,, \qquad \underline{\underline{\mathbf{S}}}(\underline{\mathbf{R}},t) = \underline{\underline{\underline{\underline{\mathbf{s}}}}}(\underline{\mathbf{R}}) : \underline{\underline{\mathbf{T}}}(\underline{\mathbf{R}},t)\,; \tag{3}$$

$\varrho_0$ is the volume density of mass at rest and $\underline{\underline{\underline{\underline{\mathbf{s}}}}}$ is the compliance tensor of fourth rank. The latter reads for the isotropic case

$$\underline{\underline{\underline{\underline{\mathbf{s}}}}}^{\mathrm{iso}}(\underline{\mathbf{R}}) = \Lambda(\underline{\mathbf{R}})\,\underline{\underline{\mathbf{I}}}\,\underline{\underline{\mathbf{I}}} + M(\underline{\mathbf{R}})\left(\underline{\underline{\mathbf{I}}}\,\underline{\underline{\mathbf{I}}}^{1324} + \underline{\underline{\mathbf{I}}}\,\underline{\underline{\mathbf{I}}}^{1342}\right) \tag{4}$$

$$\text{with} \quad \Lambda(\underline{\mathbf{R}}) = \frac{\lambda(\underline{\mathbf{R}})}{2\mu(\underline{\mathbf{R}})\left[3\lambda(\underline{\mathbf{R}}) + 2\mu(\underline{\mathbf{R}})\right]}\,, \qquad M(\underline{\mathbf{R}}) = \frac{1}{4\mu(\underline{\mathbf{R}})}\,; \tag{5}$$

$\lambda$, $\mu$ are Lamé's constants and $\underline{\underline{\mathbf{I}}}$ is the unit dyadic or the idem factor.

## EFIT Modeling of Ultrasonic Waves in Concrete

For the numerical time domain (TD) modeling of elastic waves in concrete we use the Elastodynamic Finite Integration Technique (EFIT) [3, 4].

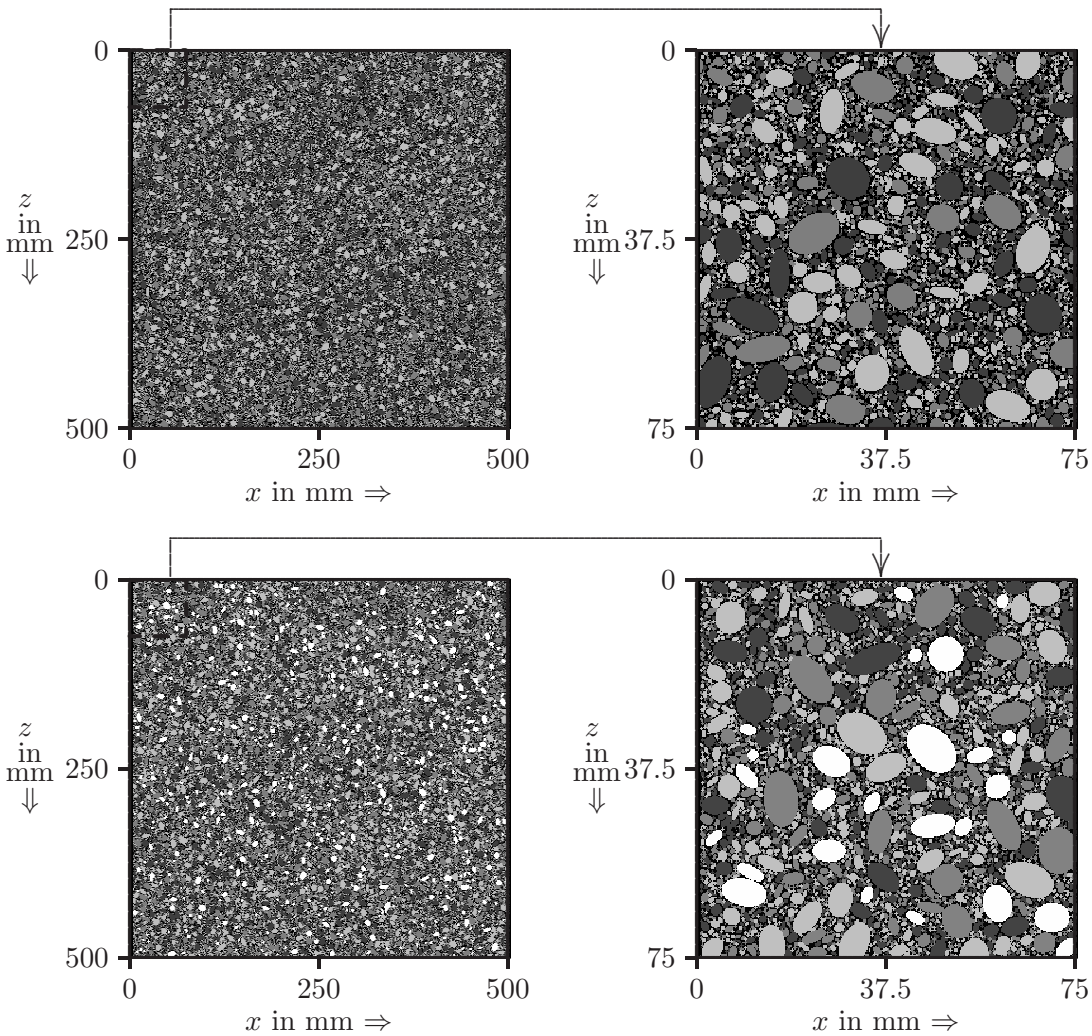


Figure 1. Left side: concrete models of the size 50 cm×50 cm for EFIT modeling; right side: detail drawings of the size 7.5 cm×7.5 cm; top: without air inclusions; bottom: with air inclusions (white ellipses); mesh size 2,000×2,000 with $\Delta x$=$\Delta z$=250$\mu$m.

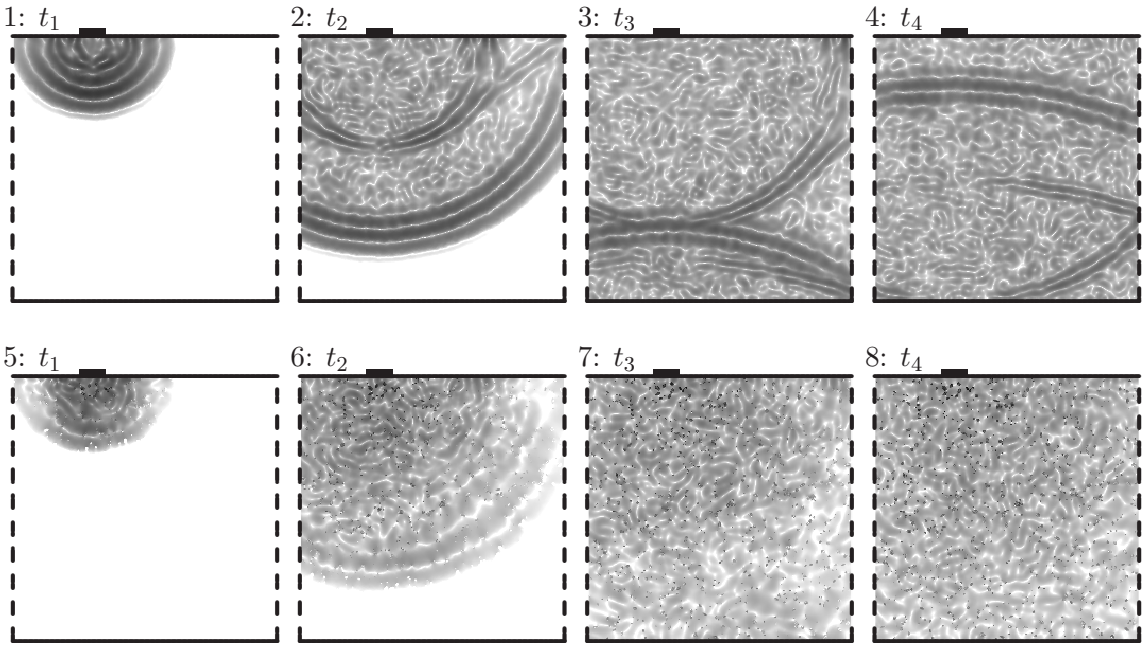


Figure 2. EFIT-$|\underline{\mathbf{v}}|$-snapshots of the elastic wavefield in concrete; cement with biatitgranite, basalt, and plaster (max. aggregate size 8mm, grading curve B8); top (1-4): without air inclusions; bottom (5-8): with air inclusions (appearing as black dots).

First applications of the numerical modeling of ultrasonic waves in concrete and an inverse scattering algorithm can be found in [4]. Due to the additives and air inclusions which may occur the material concrete is very inhomogeneous. Usually concrete consists of cement and several additives like basalt, plaster, and biatitgranite. We modeled two different situations: (1) concrete without air inclusions and (2) concrete with air inclusions. Fig. 1 illustrates the used concrete models. The base material is cement and the additives used are basalt, plaster, and biaitgranite with a max. aggregate size of 8mm. We used the grading curve B8. The additives are modeled by ca. 60,000 ellipses which are varying statistically in size, orientation and additives (see Fig. 1, right). Details can be found in [5]. Every material cell of the EFIT grid can cover different material parameters [3]. From a numerical point of view the total number of the ellipses is only limited by the number of material cells. In this example we have with a cell size of $\Delta x$=$\Delta z$=250$\mu$m a mesh size of 2,000×2,000 with $4\times10^6$ material cells. The detail drawings at the right side of Fig. 1 show clearly the statistical distribution of the ellipses. We used a normal pressure probe which has a diameter of $D$=5cm and a center frequency of $f_c = 80$ kHz in the pulse-echo technique. The time history of the probe is modeled by a raised cosine with two cycles. For EFIT modeling we applied a stress-free boundary condition on the top and bottom surface and an open boundary condition (Higdon) at the left and right boundary in order to model a infinite concrete structure. Snapshots of the elastic wavefield for both cases are shown in Fig. 2. We recognize in Fig. 2.1 and Fig. 2.5 at $t_1$ the near-field of the excited elastic wavefield. In Fig. 2.2 at $t_2$ we identify a prominent pressure wave followed by a shear wave, head waves, and Rayleigh waves at the top surface. In the case with air inclusions (Fig. 2.6 - Fig. 2.8) the wavefield is totally distorted because of multiple reflections and mode conversion effects on the air inclusions. Due to the open boundary condition reflections and mode conversions are suppressed at the vertical boundaries. The backwall echo of the pressure wave shows up very clearly only in Fig. 2.3 at $t_3$, which then propagates back to the top surface, and it is recorded by the normal pressure probe (Fig. 2.4). Only in concrete without air inclusions the traveling time of the backwall echo can then be analysed, e.g. for thickness determination.

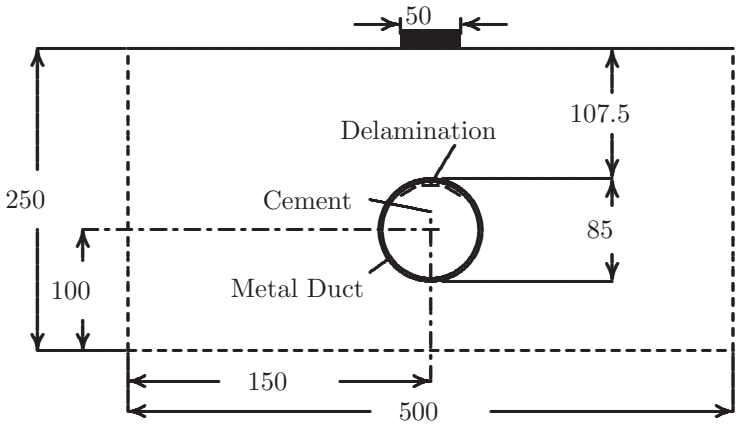

Figure 3. Geometry of the concrete with a metal duct filled with cement.

## Elastodynamic Vector Inverse Scattering: Detection of Delaminations in a Metal Duct

For inverse scattering in elastodynamics we formulated an elastic vector imaging algorithm which is called ELastic Fourier Transform Synthetic Aperture Focusing Technique (EL-FT-SAFT). It is based on the linear elastic far-field inversion including a near-field far-field transformation. The formulation of the diffraction imaging algorithm is based on Huygens' principle. Application of the equivalence principle leads to a representation of the scattered field on the surface $S$. The particle displacement vector of the scattered field is then represented by

$$\underline{\mathbf{u}}^{\mathrm{sc}}(\underline{\mathbf{R}},\omega) = \oiint_S \left\{ \underline{\mathbf{u}}(\underline{\mathbf{R}}',\omega)\cdot\left[\underline{\mathbf{n}}'\cdot\underline{\underline{\underline{\mathbf{\Sigma}}}}'(\underline{\mathbf{R}}-\underline{\mathbf{R}}',\omega)\right] - \underline{\mathbf{n}}'\cdot\underline{\underline{\mathbf{T}}}(\underline{\mathbf{R}}',\omega)\cdot\underline{\underline{\mathbf{G}}}(\underline{\mathbf{R}}-\underline{\mathbf{R}}',\omega)\right\}\mathrm{d}\,S'\,. \tag{6}$$

with $\underline{\mathbf{n}}'$ as the outward normal unit vector of the surface $S$, $\underline{\underline{\underline{\mathbf{\Sigma}}}}$ is the triadic and $\underline{\underline{\mathbf{G}}}$ the dyadic displacement Green's function of free space. Introducing far-field approximation in (6) we get the definition of the linearized far-field scattering amplitude for perfect scatterer $\underline{\mathbf{C}}_{\alpha\beta}(\hat{\underline{\mathbf{R}}},\omega)$. Then, in linear physical elastodynamics (PE) the singular function of a perfect scatterer is given by the elastodynamic Fourier diffraction slice theorem in the K-space here for the bistatic case (bi) [6]

$$\widetilde{\gamma}_u^{\mathrm{E}}(\underline{\mathbf{K}}) = \frac{\underline{\mathbf{V}}_{\alpha\beta}^{\mathrm{PE,bi}}(\hat{\underline{\mathbf{R}}},\hat{\underline{\mathbf{k}}}_i,\omega)}{|\underline{\mathbf{V}}_{\alpha\beta}^{\mathrm{PE,bi}}(\hat{\underline{\mathbf{R}}},\hat{\underline{\mathbf{k}}}_i,\omega)|^2}\frac{e^{-\mathrm{j}\,K_{z\beta}d}}{4\pi}\left[\widetilde{\underline{\mathbf{u}}}_\alpha(\mathrm{K}_x,\mathrm{K}_y,d,\omega)\,\underline{\mathbf{e}}_z : \underline{\underline{\underline{\mathbf{\Sigma}}}}_\beta(\hat{\underline{\mathbf{R}}},\omega)\right.$$
$$\left. -\underline{\mathbf{e}}_z\cdot\underline{\underline{\widetilde{\mathbf{T}}}}_\alpha(\mathrm{K}_x,\mathrm{K}_y,d,\omega)\cdot\underline{\underline{\mathbf{G}}}_\beta(\hat{\underline{\mathbf{R}}},\omega)\right]\,, \qquad \alpha,\beta = \mathrm{P},\,\mathrm{S}\,. \tag{7}$$

This equ. (7) represents the essence of the elastodynamic vector imaging algorithm EL-FT-SAFT. As an example, we consider the following question: „Is it possible to detect delaminations in a metal duct which is filled with cement"? Fig. 3 shows the geometry of a concrete sample with a metal duct which has three delaminations. The EFIT modeled wavefield is given in Fig. 4, on the left hand side without delaminations and on the right hand side with delaminations. In the latter case the reflected pressure wave from the metal duct (delaminations) has a higher amplitude. For each situation we „recorded" a rf-data field in a finite aperture, which is indicated by the black bar in Fig. 3. Then we applied the EL-FT-SAFT imaging scheme to the pressure and shear part in order to get a P-image and S-image separately. The images are shown in Fig. 5, left and middle. The superposition of the P- and S-image to a PS-image is given on the right hand side of Fig. 5. We clearly recognize an improvement in the PS-image. Nevertheless, it is not possible to image the delaminations itself. We get only an indication of the delaminations because of the higher amplitude in the reconstruction of the upper part of the metal duct.

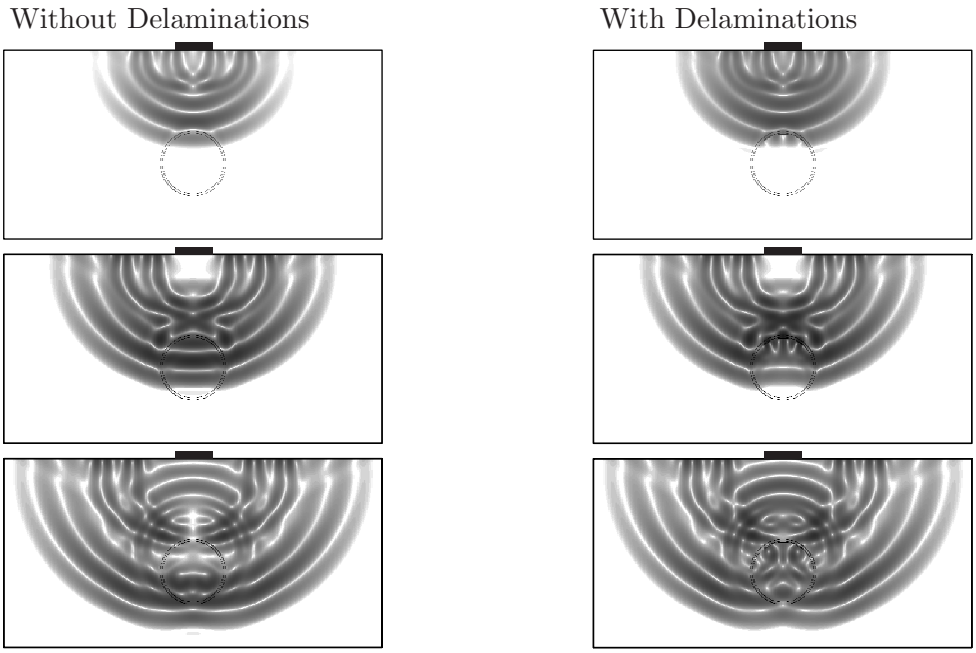


Figure 4. EFIT-$|\underline{\mathbf{v}}|$-snapshots of the elastic wavefield in concrete with metal duct; left without and right with delaminations; the probe is indicated by the black bar.

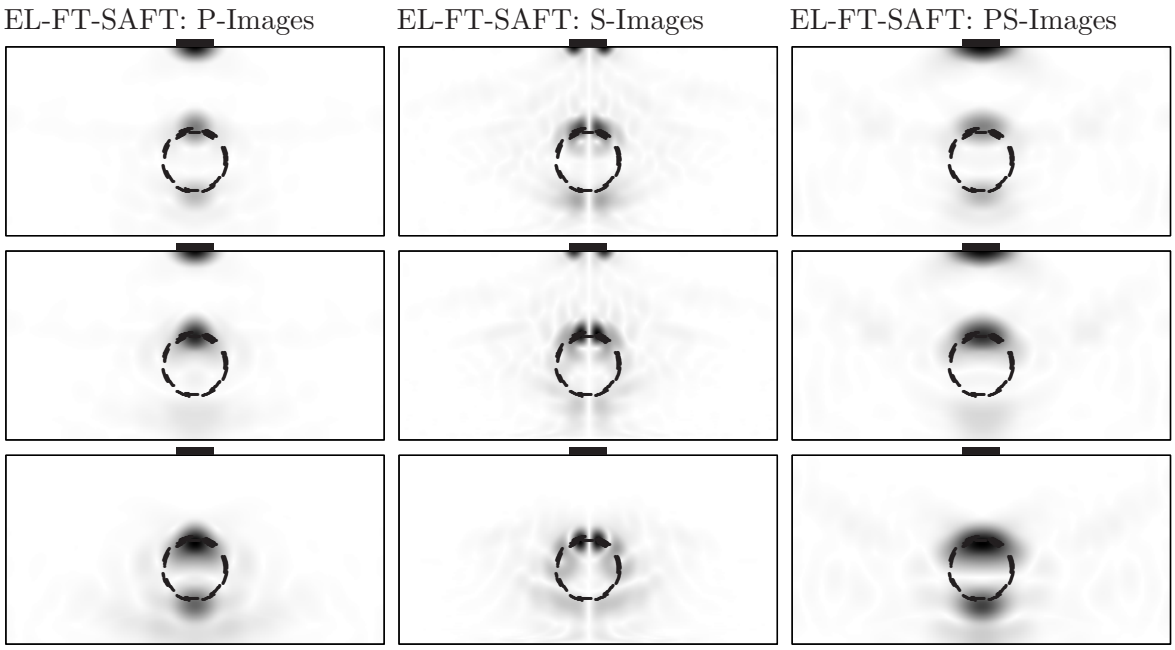


Figure 5. EL-FT-SAFT reconstructions; from the top to the bottom: without delaminations (1), with delaminations (2), scattered field (2 minus 1).

## ELECTROMAGNETIC WAVES APPLIED TO CONCRETE

Electromagnetic waves are governed by Maxwell's equation [7]. These read in integral form for a finite surface $S$ with the contour $C$

$$\iint_S \frac{\partial}{\partial t}\underline{\mathbf{B}}(\underline{\mathbf{R}},t)\cdot\underline{\mathbf{n}}\,\mathrm{d}S = -\oint_C \underline{\mathbf{E}}(\underline{\mathbf{R}},t)\cdot\underline{\mathbf{s}}\,\mathrm{d}R\,, \tag{8}$$

$$\iint_S \frac{\partial}{\partial t}\underline{\mathbf{D}}(\underline{\mathbf{R}},t)\cdot\underline{\mathbf{n}}\,\mathrm{d}S = \oint_C \underline{\mathbf{H}}(\underline{\mathbf{R}},t)\cdot\underline{\mathbf{s}}\,\mathrm{d}R - \iint_S \underline{\mathbf{J}}(\underline{\mathbf{R}},t)\cdot\underline{\mathbf{n}}\,\mathrm{d}S\,; \tag{9}$$

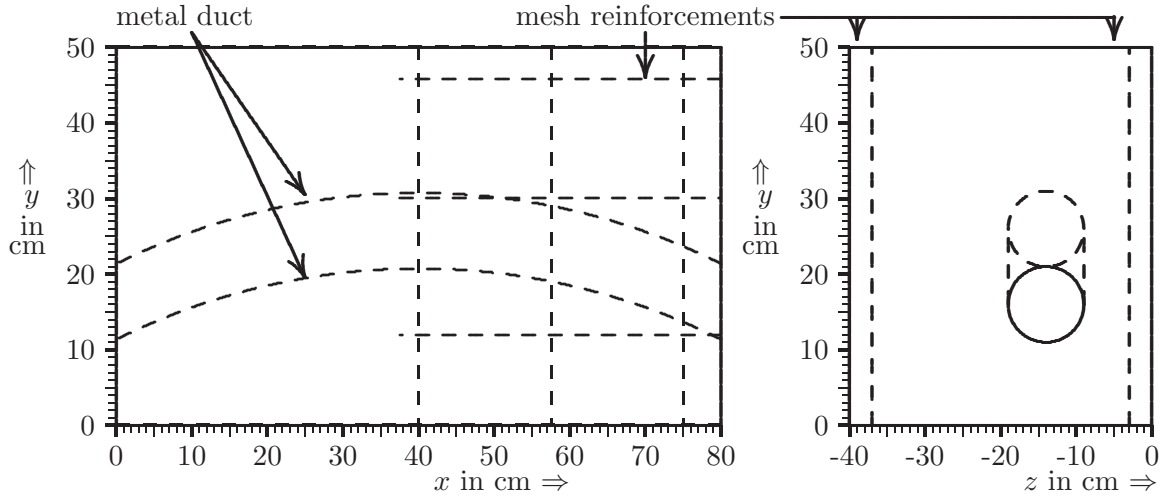


Figure 6. Reinforced concrete sample with a size of 80cm×50cm×40cm ($\varepsilon_{\rm r} \simeq 7$) with an embedded metal duct (9cm deep) and mesh reinforcements (3cm and 37cm deep).

$\underline{\mathbf{B}}$ is the magnetic flux density vector, $\underline{\mathbf{E}}$ is the electric field, $\underline{\mathbf{D}}$ is the electric flux density vector, $\underline{\mathbf{H}}$ is the magnetic field, $\underline{\mathbf{J}}$ is the electric current density vector, $\underline{\mathbf{n}}$ is the outward normal unit vector of $S$ and $\underline{\mathbf{s}}$ is the tangential vector of $C$. We model concrete as a non-magnetic non-dissipative isotropic material which is homogeneous with respect to the relative permittivity $\varepsilon_{\rm r}$. Then the electromagnetic constitutive equations are the following

$$\underline{\mathbf{B}}(\underline{\mathbf{R}},t) = \mu_0 \underline{\mathbf{H}}(\underline{\mathbf{R}},t)\,, \qquad \underline{\mathbf{D}}(\underline{\mathbf{R}},t) = \varepsilon_{\rm r}\varepsilon_0 \underline{\mathbf{E}}(\underline{\mathbf{R}},t)\,; \tag{10}$$

$\mu_0$ is the permeability and $\varepsilon_0$ is the permittivity of free space. The phase velocity in concrete is $c_{\rm ph}^{\rm con} = 1/\sqrt{\mu_0\varepsilon_{\rm r}\varepsilon_0} = c_0/\sqrt{7}$=1.134×10$^8$ m/s The relative permittivity of concrete is $\varepsilon_{\rm r} \simeq 7$. This yields at center frequency a phase velocity of $c_{\rm ph}^{\rm con}$= $c_0/\sqrt{7}$=1.134×10$^8$ m/s and a wave length of $\lambda_{\rm c}^{\rm con} = 12.6$ cm.

Electromagnetic Vector Inverse Scattering: Location of a Metal Duct

Fig. 6 shows a typical reinforced concrete sample with a metal duct (9cm deep, diameter D=10cm) and mesh reinforcements (3cm and 37cm deep, mesh size 18cm) which is applied to both sides of half the sample. The metal duct is filled with cement. Tendons are not incorporated here. Important parameters of the concrete are: strength category B45; portland blastfurnace cement HOZ35L; grading curve AB8; total water/cement ratio 0.48. We assume that the metal duct and mesh reinforcement are perfect conductors with infinite conductivity ($\sigma \to \infty$). In order to locate the metal duct in the reinforced concrete we applied a commercial ground probing pulsed radar. We measured 21×498 points in $xy$-plane, each point has 512 time samples. Then we applied a linear interpolation in $x$-direction and we took every sixth sample in $y$-direction. This yields a 3D data field of 121×84×512 samples. The measurements have been made by Dr. Maierhofer at the Bundesanstalt für Materialforschung und -prüfung (BAM) in Berlin/Germany. The antenna is a microstrip butterfly antenna of the size 18 cm × 32 cm with a center frequency of $f_{\rm c} = 900$ MHz and a bandwidth of B=1 GHz (see Fig. 7). The butterfly antenna can be approximated by an electric dipole $\underline{\mathbf{p}} = p_0(\omega)\underline{\hat{\mathbf{p}}}$ with the unit vector $\underline{\hat{\mathbf{p}}}$ and spectrum $p_0(\omega)$. The excitation pulse is a time derivated Gaussian function. For linear physical optics (PO) (Kirchhoff approximation) we write down the following vector backprojection algorithm in the time domain for the illuminated top surface of the singular function

$$\gamma_u^{\rm EM}(\underline{\mathbf{R}}) = \frac{8\sqrt{\varepsilon_{\rm r}}}{Z_0\, c_0} \iint_{S_M} \frac{(\underline{\mathbf{R}}' - \underline{\mathbf{R}})\cdot\underline{\mathbf{n}}'}{|\underline{\mathbf{R}} - \underline{\mathbf{R}}'|^2 - \left[\underline{\hat{\mathbf{p}}}\cdot(\underline{\mathbf{R}} - \underline{\mathbf{R}}')\right]^2} \underline{\hat{\mathbf{p}}}\cdot\underline{\mathbf{E}}^{\rm sc}(\underline{\mathbf{R}}', \widetilde{t} = 2\sqrt{\varepsilon_{\rm r}}|\underline{\mathbf{R}} - \underline{\mathbf{R}}'|/c_0)\mathrm{d}S'\,. \tag{11}$$

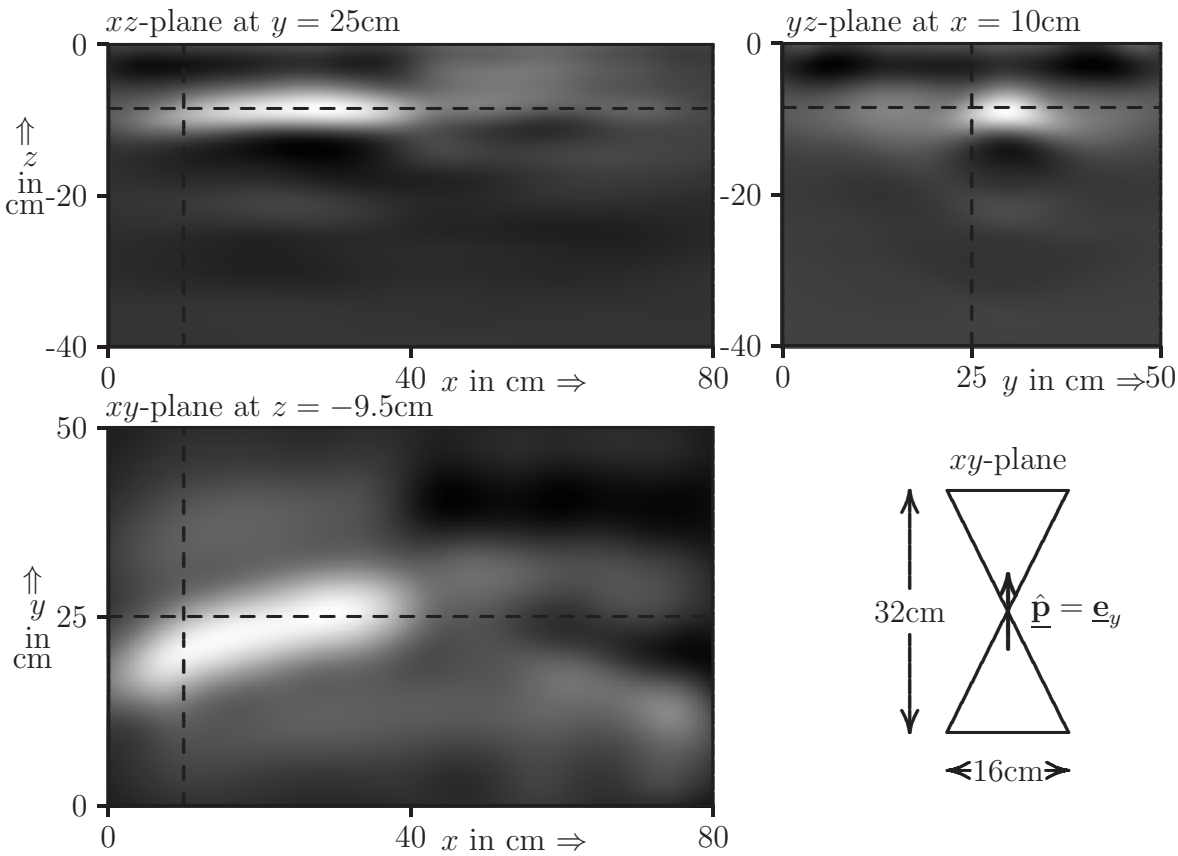


Figure 7. Three orthogonal slices of the reconstructed illuminated top surface of the singular function $\gamma_u^{\mathrm{EM}}(\underline{\mathbf{R}})$, showing the metal duct in the reinforced concrete. Lower right: geometry of the microstrip butterfly antenna.

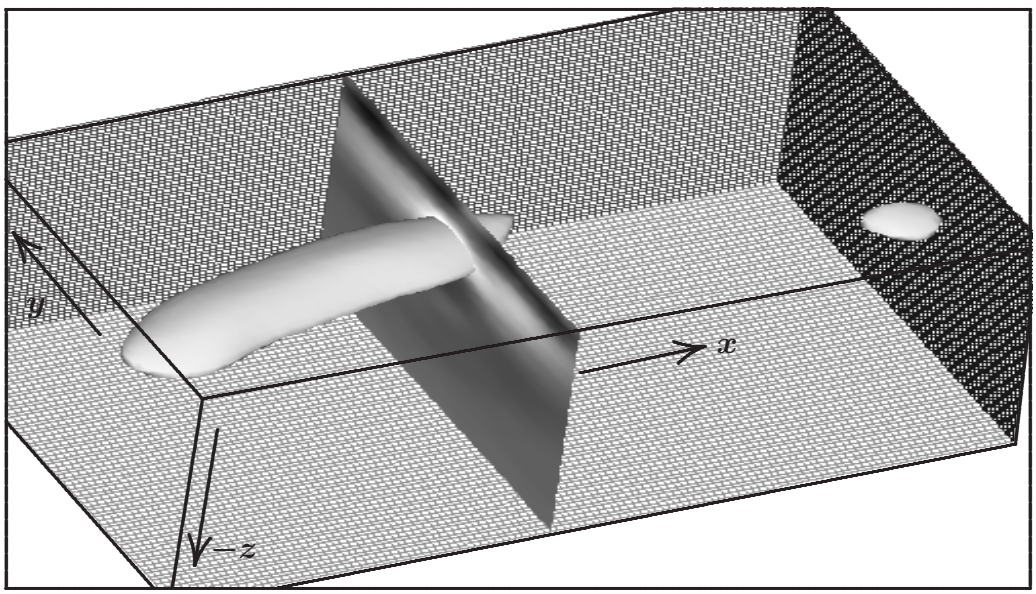


Figure 8. Isosurface of the reconstructed illuminated top surface of the singular function $\gamma_u^{\mathrm{EM}}(\underline{\mathbf{R}})$, showing the metal duct in the reinforced concrete.

This inversion scheme is called Hertzian Dipole Physical Optics Far-Field Inverse Scattering (HD-POFFIS) [8]. A scalar version of POFFIS can be found in [9] and for further reading about inverse scattering see [10, 11, 12]. We applied the formula (11) to measurements of the concrete sample shown in Fig. 6. Fig. 7 shows three orthogonal slices and Fig. 8 shows an isosurface of the reconstructed illuminated top surface of the singular function. Both figures represent a good agreement with the given real geometry of the metal duct (see Fig. 3). Because of shielding effects of the mesh reinforcement on the right half of the sample, the right part of the metal duct is missed in the reconstruction. To test the influence of the vector character of this inversion scheme we made a further reconstruction with a purposely wrong dipole direction $\hat{\underline{\mathbf{p}}} = \underline{\mathbf{e}}_x$. This leads to defocusing effects which are also present if we use a scalar FT-SAFT imaging algorithm [13, 14].

## CONCLUSIONS

We have presented the numerical modeling of ultrasonic waves in concrete with the EFIT code. The highly inhomogeneous material concrete has been modeled by a statistically varying distribution of ellipses. A typical number is 60,000. By the combination of time domain EFIT modeling and the elastodynamic vector imaging scheme EL-FT-SAFT it has been shown that it is possible to detect delaminations in a metal duct with the application of ultrasonic waves. We have documented the resulting improvement in the reconstruction by using the elastodynamic vector inversion scheme. Finally, we have shown the application of the electromagnetic vector imaging scheme HD-POFFIS to measured data in order to detect a metal duct embedded in reinforced concrete taking into account the vector character of electromagnetic waves.

## REFERENCES


[1] B. A. Auld, *Acoustic Fields and Waves in Solids*, Krieger, Malabar (1990)

[2] J. H. M. T. van der Hijden, *Propagation of Transient Elastic Waves in Stratified Anisotropic Media*, North-Holland, Amsterdam (1987)

[3] P. Fellinger, R. Marklein, K. J. Langenberg, S. Klaholz, Wave Motion **21** (1995) pp. 47-66

[4] R. Marklein, R. Bärmann, K. J. Langenberg, in: Review of Progress in Quantitative Nondestructive Evaluation 1994, eds.: D. O. Thompson, D. E. Chimenti, **14**, Plenum Press, New York (1995) pp. 251-258

[5] S. Irmer, H. Müller, Report, University of Kassel, Kassel (1995)

[6] R. Bärmann, K. J. Langenberg, in: Advances in Acoustic Microscopy 2, eds.: G. A. D. Briggs, W. Arnold, Oxford University Press, Oxford (to be published)

[7] H. C. Chen, *Theory of Electromagnetic Waves: A Coordinate-Free Approach*, McGraw-Hill, New York (1983)

[8] M. Brandfaß, Ph. D. Thesis, University of Kassel, Kassel (1995)

[9] N. N. Bojarski, IEEE Trans. Ant. Propagat. **AP-30** (1982) pp. 980-989

[10] M. Brandfaß, K. J. Langenberg, in: Review of Progress in Quantitative Nondestructive Evaluation 1991, eds.: D. O. Thompson, D. E. Chimenti, **11**, Plenum Press, New York (1992) pp. 741-748

[11] K. J. Langenberg, Wave Motion **11** (1989) pp. 99-112

[12] K. J. Langenberg, M. Brandfaß, P. Fellinger, T. Gurke, T. Kreutter, in: Radar Target Imaging, eds.: W. M. Boerner, H. Überall, Springer-Verlag, Berlin (1994) pp. 113-151

[13] K. Mayer, R. Marklein, K. J. Langenberg, T. Kreutter, Ultrasonics **28** (1990) pp. 241-255

[14] K. J. Langenberg, P. Fellinger, R. Marklein, P. Zanger, K. Mayer, T. Kreutter, in: Evaluation of Materials and Structures by Quantitative Ultrasonics, ed. : J. D. Achenbach, Springer-Verlag, Vienna (1993) pp. 317-398